Synthesis of Metastable Phases in the Magnesium Spinel−Alumina System

T. R. Hinklin*,† and R. M. Laine

Department of Materials Science and Engineering, University of Michigan, Ann Arbor, Michigan 48109-2136

Received August 22, 2007. Revised Manuscript Received November 2, 2007

We report here the use of liquid-feed flame spray pyrolysis to produce 14 nanopowders along the Al_2O_3−$MgAl_2O_4$ tie-line by combusting varied ratios of aerosolized ethanol solutions of alumatrane [$Al(OCH_2CH_2)_3N$] and magnesium acetylacetonate [$Mg(C_5H_7O_2)_2$]. The resulting nanopowders were characterized by X-ray fluorescence, N_2 adsorption (Brunauer−Emmett−Teller), scanning electron microscopy, X-ray diffraction (XRD), and Fourier transform infrared (FTIR) spectroscopy. The powders typically consist of single-crystal particles of <30 nm diameter and specific surface areas of 30–80 m^2/g. Complementary XRD and FTIR studies show a gradual change in the powder patterns and spectra from δ-Al_2O_3 to $MgAl_2O_4$. Intermediate compositions exhibit phases that fall well outside of the established phase diagram and provide insight into the structure of transition aluminas. These materials have been shown to exhibit novel photonic behavior and have potential value as a new catalyst or support.

Introduction

The magnesium aluminate spinel−alumina binary phase system includes materials used for many important industrial applications including catalyst–supports, refractories, abrasives, and transparent, high strength, and radiation-tolerant ceramics.[1–7] Recently, the catalytic use of magnesium aluminate spinels has received significant attention as an alternative to traditional alumina-supported catalysts because of its high thermal stability and strong bacisity.[8] The ability to generate ultrafine or nanosized powders of controlled chemical and phase composition along the $(MgO)_x(Al_2O_3)_{1-x}$ tie-line offers the opportunity to tune the desired properties for these current applications. Typically, ultrafine oxides are produced by the sol–gel route,[9] chemical precipitation,[10] or similar processes;[11,12] however, these methods often require calcination to produce the desired crystalline phases. In contrast, the use of aerosol combustion techniques offers a direct route to crystalline unaggregated nanomaterials and phases not accessible by the more traditional routes.[13] Furthermore, unaggregated nanosized powders may offer novel properties in their own right in addition to easier processing for all applications.

Liquid-feed flame spray pyrolysis (LF-FSP) is a highly flexible tool that allows for the development of nanosized, nonporous, unaggregated, mixed-metal oxides of controlled composition.[14–18] LF-FSP offers access to known phases as well as difficult or impossible to access phases and phase compositions.[19,20] On the basis of the flexibility of LF-FSP, we report here systematic tailoring along the $MgAl_2O_4$−Al_2O_3 tie-line as a means to access nanopowders with complete control of the chemical composition. These materials, especially those with unusual phases or phase compositions, may offer properties hitherto unknown for this extremely well-studied system.

We are particularly interested in developing these materials to create transparent fine-grained monoliths for applications ranging from transparent armor to polycrystalline lasers and infrared (IR) transparent radomes.[4,7,21] In this context, one

* Corresponding author. E-mail: thinkli@sandia.gov.
† Present address: Sandia National Laboratories, 1001 University Boulevard, Albuquerque, New Mexico 87106.

(1) Guo, J.; Lou, H.; Zhao, H.; Chai, D.; Zheng, X. *Appl. Catal., A* **2004**, *273*, 75.
(2) Ghosh, A.; Ritwik, S.; Mukherjee, B.; Das, S. K. *J. Eur. Ceram. Soc.* **2004**, *24*, 2079.
(3) Bhaduri, S.; Bhaduri, S. B. *Ceram. Int.* **2002**, *28*, 153.
(4) Ghosh, A.; White, K. W.; Jenkins, M. G.; Kobayashi, A. S.; Bradt, R. C. *J. Am. Ceram. Soc.* **1991**, *74*, 1624.
(5) Devanathan, R.; Yu, N.; Sickafus, K. E.; Nastasi, M. *J. Nucl. Mater.* **1996**, *232*, 59.
(6) Chauvin, N.; Albiol, T.; Mazoyer, R.; Noirot, J.; Lespiaux, D.; Dumas, J. C.; Weinberg, C.; Ménard, J. C.; Ottaviani, J. P. *J. Nucl. Mater.* **1999**, *274*, 91.
(7) Ginley, D. S.; Bright, C. *MRS Bull.* **2000**, *25* (8), 15.
(8) Salmones, J.; Galicia, J. A.; Wang, J. A.; Valenzuela, M. A.; Aguilar-Rios, G. *J. Mater. Sci. Lett.* **2000**, *19*, 1033.
(9) Dutoit, D. C. M.; Schneider, M.; Baiker, A. *J. Catal.* **1995**, *153* (1), 165.
(10) Zawrah, M. F.; Hamad, H.; Meky, S. *Ceram. Int.* **2007**, *33* (6), 969.
(11) Meyer, F.; Hempelmann, R.; Mathur, S.; Veith, M. *J. Mater. Chem.* **1999**, *9* (8), 1755.
(12) Yamaguchi, O.; Taguchi, H.; Shimizu, K. *Polyhedron* **1987**, *6* (9), 1794.
(13) Madler, L.; Kammler, H. K.; Mueller, R.; Pratsinis, S. E. *J. Aerosol Sci.* **2002**, *33* (2), 369.
(14) Bickmore, C. R.; Waldner, K. F.; Treadwell, D. R.; Laine, R. M. *J. Am. Ceram. Soc.* **1996**, *79*, 1419.
(15) Hinklin, T.; Toury, B.; Gervais, C.; Babonneau, F.; Gislason, F. F.; Morton, R. W.; Laine, R. M. *Chem. Mater.* **2004**, *16*, 21.
(16) Baranwal, R.; Villar, M. P.; Garcia, R.; Laine, R. M. *J. Am. Ceram. Soc.* **2001**, *84*, 951.
(17) Marchal, J; Hinklin, T.; Baranwal, R.; Johns, T.; Laine, R. M. *Chem. Mater.* **2004**, *16*, 822.
(18) Bickmore, C. R.; Waldner, K. F.; Baranwal, R.; Hinklin, T.; Treadwell, D. R.; Laine, R. M. *J. Eur. Ceram. Soc.* **1998**, *18*, 287.
(19) Laine, R. M.; Marchal, J.; Sun, H. J.; Pan, X. Q. *Adv. Mater.* **2005**, *17*, 830.
(20) Azurdia, J. A.; Marchal, J. C.; Shea, P.; Sun, H.; Pan, X. Q.; Laine, R. M. *Chem. Mater.* **2006**, *18*, 731.
(21) Li, J. G.; Ikegami, T.; Lee, J. H.; Mori, T. *J. Am. Ceram. Soc.* **2000**, *83*, 2866.

10.1021/cm702388g CCC: $40.75
Published on Web 12/28/2007

aspect of the work reported here is to produce and characterize nanopowders with low MgO concentrations (0.1–2 mol %) to investigate their utility as homogenously doped nano-transitional aluminas for sintering to fully dense, fine-grained α-alumina monoliths, as recently described.[22] In addition, nanoalumina powders with MgO concentrations of 1–10 mol % are being investigated for novel UV emission based on defects associated with Mg^{2+} in the tetragonal alumina structure, as reported elsewhere.[23]

We have previously reported the LF-FSP production of stoichiometric nano-$MgAl_2O_4$ spinel and pure ∂-Al_20_3.[14,15] In addition to this study, similar binary compositional studies on the nickel, cobalt, zinc, and copper aluminate systems were undertaken and recently published.[20,24,25] These studies provide the basis for developing ternary, quaternary, or greater compositions for advanced photonic and catalyst applications. In this paper, we continue our efforts to develop materials of potential interest in these scientific domains. This study explores and characterizes the $Al_2O_3-MgAl_2O_4$ phase field created through LF-FSP of simple metalloorganic precursors suitable for industrial-scale production.[14–22]

Experimental Section

Materials. Magnesium acetylacetonate [$Mg(Acac)_2$, $Mg(C_5H_7O_2)_2$, 98+%], triethanolamine [$N(CH_2CH_2OH)_3$, 98%], tetrahydrofuran [THF, C_4H_8O, 99+% stabilized], and anhydrous ethanol [CH_3CH_2OH, 99$^+$%] were purchased from Alfa Aesar and used as received. Aluminum tri-*sec*-butoxide [$Al(OsBu)_3$, 97%] was purchased from Chattem Chemical Co. and used as received.

Precursor Formulations. Alumatrane {$Al[N(CH_2CH_2O)_3]$} was synthesized from $Al(OsBu)_3$ and $N(CH_2CH_2OH)_3$ as described elsewhere[14] and then diluted with ethanol such that the ceramic yield was 7.5 wt % by thermogravimetric analysis (TGA). The magnesium precursor was prepared by dissolving $Mg(Acac)_2$ in 50:50 THF/EtOH with stirring for 24 h. This solution was filtered through No. 40 filter paper (Whatman) to remove ≈0.5 wt % of the residual solids. The resulting solution was characterized by TGA for the MgO content, typically 3–4 wt %. Volumetric measurements were used to mix both the MgO and Al_2O_3 solutions with the desired stoichiometric amounts such that the final concentration of ceramic (Al_2O_3 + MgO) in solution was 2 wt % and the THF/EtOH ratio was 50:50.

LF-FSP. Precursor formulations are atomized at 50 mL/min in an ultrasonic oxygen atomizer to generate an oxygen-rich aerosol, which is ignited via methane/oxygen pilot torches in the device's ignition chamber. Combustion occurs at temperatures of up to 2000 °C, producing nanopowder and gaseous byproducts. A steep temperature gradient, >500 °C/s, between the combustion chamber and the 300 °C collection point provides rapid quenching of the powder after combustion, as the powders are carried away from the combustion area by the natural flow of gases aided by a high-velocity (>700 cfm) in-line blower. The powders are collected downstream in a pair of 6 ft. × 3 in. wires in electrostatic precipitator (ESP) tubes maintained at a 10 kV pseudo-direct-current potential. After the run is complete, powders are recovered from the ESP tubes and stored in plastic bags. Other descriptions of this technique have been published elsewhere.[14]

X-ray Diffraction (XRD). The phases and crystallite sizes of as-prepared samples were characterized by XRD, using a Rigaku rotating-anode goniometer (Rigaku Denki Co. Ltd., Tokyo, Japan). Powder samples for the Rigaku diffractometer were prepared by pressing ≈100 mg in amorphous silica slides for data collection. Cu Kα (λ = 1.54 Å) radiation with a Ni filter was used with a working voltage and a current of 40 kV and 100 mA, respectively. Scans were continuous from 10 to 80° 2θ with a step scan of 2° 2θ/min and increments of 0.05° 2θ. Scan data were processed using Jade software version 7.0 (Materials Data, Inc., Livermore, CA). The processing included phase determination, crystallite size, and unit cell dimensions.

Diffuse-Reflectance Infrared Fourier Transform (DRIFT) Spectroscopy. DRIFT spectra were recorded on a Mattson Galaxy series 3000 Fourier transform infrared (FTIR) spectrometer (Mattson Instruments, Inc., Madison, WI). Optical-grade, random cuttings of KBr (International Crystal Laboratories, Garfield, NJ) were ground using an alumina mortar and pestle, with 1.0 wt % of the sample to be analyzed and packed firmly in the sample holder and leveled off at the upper edge to provide a smooth surface. Samples were transferred to the FTIR sample chamber, which was flushed continuously with N_2. Each spectrum is continuous in the range of 4000–400 cm^{-1} with a scan resolution of 4 cm^{-1} with an average of 128 scans.

Specific Surface Area (SSA) Analysis. SSAs were obtained using a Micromeritics ASAP 2010 sorption analyzer (Norcross, GA). Samples (200 mg) were degassed at 400 °C for 2 h or until the degas rate was less than 0.005 Torr. Analysis was conducted at −196 °C (77 K) with N_2 as the adsorbate gas. The SSAs were determined by the Brunauer−Emmett−Teller (BET) multipoint method using at least five data points with relative pressures of 0.001–0.20. The particle's average size was derived from the formula

$$\langle D \rangle = 6/\rho(\mathrm{SSA})$$

Scanning Electron Microscopy (SEM). A field-emission SEM (Philips model XL-30) was used to image powder morphologies. Powder samples were prepared by dispersing the powder (0.1 g) in distilled water (10 mL). A drop of the suspension was placed on a polished aluminum stub and allowed to dry. The dried powder films were spark-coated with a thin film of carbon to reduce charging effects. An operating voltage of 30.0 kV was used with a spot size of 3.

X-ray Fluorescence (XRF). Samples were prepared by mixing a 0.50 g sample in 10.0 g of a $Li_2B_4O_7$ glass flux. The sample and glass flux were mechanically stirred for 5 min in a methacrylate vial with three methacrylate balls using a SPEX 6000 ball mill. The mixtures were fused into glass beads by placing them in an oven held at 1000 °C for 10 min. The samples were analyzed using a Panalytical PW2400 XRF spectrometer (formerly Philips), equipped with a WDS detection system (wavelength dispersive).

Results and Discussion

We report here the synthesis and characterization of a series of samples that lie along the $MgAl_2O_4-Al_2O_3$ tie-line. These nanopowder materials were produced in a single-step process, bypassing the more labor-intensive and costly routes typically used to synthesize similar materials. We have previously demonstrated that LF-FSP processing provides compositions that are otherwise hard or impossible to attain.[17–22,25] Here we continue a series of studies demonstrating that LF-FSP is a highly effective process for developing metastable materials with the spinel crystal structure that lie well outside the thermodynamic phase field. In addition, as-produced low MgO concentration and stoichio-

(22) Laine, R. M.; Marchal, J. C.; Sun, H. P.; Pan, X. Q. *Nat. Mater.* **2006**, *5*, 710.
(23) Li, B.; Oliveira, S. L.; Rand, S. C.; Azurdia, J. A.; Hinklin, T. R.; Marchal, J. C.; Laine, R. M. *J. Appl. Phys.* **2007**, *101*, 053534.
(24) Azurdia, J. A.; Marchal, J. C.; Laine, R. M. *J. Am. Ceram. Soc.* **2006**, *89*, 2749.
(25) Laine, R. M.; Hinklin, T. R.; Azurdia, J.; Kim, M.; Marchal, J. C.; Kumar, S. *Adv. Mater.* **2007**,accepted for publication.

Table 1. $MgO-Al_2O_3$ Compositions as Target mol % MgO Compared to XRF Values of Those Produced by LF-FSP, with Their Average Particle Diameters by SSA and XRD Line Broadening

	mol % MgO													
	0	0.1	0.2	0.5	1	2.5	5	6.06	7.17	10	20	30	40	50
SSA (nm)	25	23	26	24	24	28	31	28	28	26	29	26	29	32
XRD (nm)	11	10	11	12	12	16	16	17	17	20	26	23	21	28
XRF (mol %)	0	0.06	0.22	0.49	1.03	2.44	4.74	5.91	7.09	10.1	20.5	29.6	40.2	49.8

metric spinel nanopowders, with effective ceramic processing, can be sintered to high densities with retained fine microstructures, as will be reported elsewhere.

Nanopowders made by traditional solution techniques tend to be hydrates or amorphous or contain micropores.[9,11] In this study, all samples exhibit relatively high surface areas (Table 1), have no microporosity, and exhibit faceted-spherical morphology. These features also combine controlled stoichiometry with a high degree of crystallinity, making them excellent candidates for catalytic and photonic applications. The lack of micropores and their very high thermal stability[20] suggest that these materials will likely retain their catalytic properties even after exposure to high-temperature or -pressure environments. When these materials are doped with the appropriate ions, their high degree of crystallinity should offer ideal emission behavior without the need for annealing or calcination, as is typically required for phosphors made by alternative routes.[23,26]

In the following sections, we discuss the formulation of precursors and nanopowder production. We then discuss the series of produced nanopowders in terms of crystalline phases present, their SSAs, the dominant metal–oxygen coordination, and morphology.

Precursor Formulations

A set of 14 precursor formulations (Table 1) was prepared by mixing precise amounts of alumatrane, $Al[N(CH_2CH_2O)_3]$, and magnesium, $Mg(Acac)_2$, precursors. The solutions were diluted with THF/EtOH and mechanically stirred for 1 h prior to powder synthesis. All solutions were formulated to contain 2 wt % ceramic yield in order to minimize complications with the LF-FSP process, such as solubility differences, and to ensure a constant flux density of metal oxide species in the flame.

Powder Characterization

The compositions reported here are the targeted compositions. Based upon the calibration curve established, using the WDS XRF values, the targeted and measured compositions are within the assumed error of ±2% (Table 1).

The average particle sizes (APSs) calculated from SSA analyses of all of the as-produced samples are shown in Table 1. The APS is roughly constant with an increase in the MgO content to stoichiometric $MgAl_2O_4$. The difference in density between stoichiometric spinel (3.6 g/cm^3) and pure δ-alumina (3.6 g/cm^3) is negligible and is assumed to not vary significantly with the incorporation of the Mg ions into the $Mg_xAl_{2-x}O_4$ matrix. No microporosity was expected or detected in any sample.

The APS values obtained by Debye−Scherer XRD line-broadening analyses are shown in Table 1. APS values obtained by XRD increase with an increase in the MgO content. This is likely due to the presence of additional phases at low MgO contents (Figure 3) and the documented small domain structure of the transition aluminas.[34] The APS of all powders is <30 nm regardless of the technique used to calculate the values.

SEM

SEMs of all samples were taken in order to study particle morphology. Figure 1 shows micrographs of the 0 mol % $MgO-Al_2O_3$, 0.5 mol % $MgO-Al_2O_3$, 2.5 mol % $MgO-Al_2O_3$, 5 mol % $MgO-Al_2O_3$, 30 mol % $MgO-Al_2O_3$, and 50 mol % $MgO-Al_2O_3$ samples, which are representative of all other samples. The powders exhibit homogeneous spherical morphologies, and also evident is the narrow particle size distribution; however, the exact size distribution was not determined by an analytical technique. The APSs of the particles are clearly <60 nm, in reasonable agreement with the results obtained by BET and XRD. The amount of coalesced secondary particles increases with an increase in the MgO content likely because of the change in the LF-

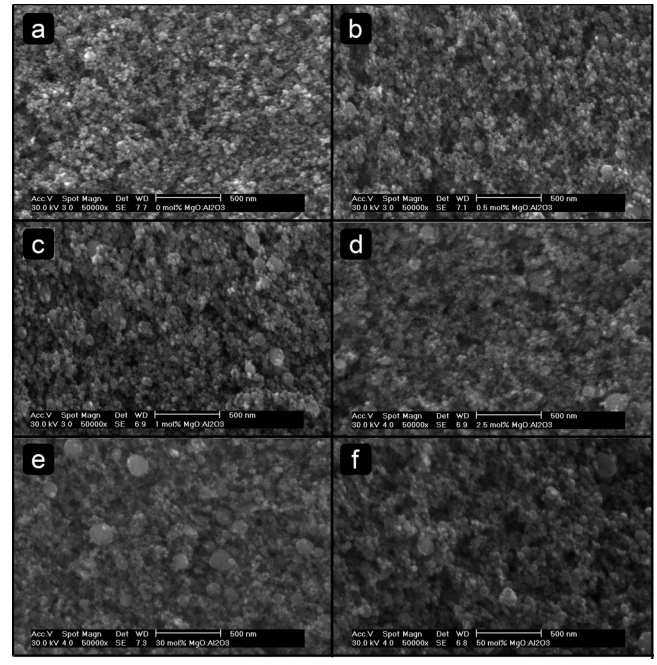

Figure 1. SEM images of as-produced $MgO-Al_2O_3$ powders: (a) 0 mol % $MgO-Al_2O_3$; (b) 0.5 mol % $MgO-Al_2O_3$; (c) 1 mol % $MgO-Al_2O_3$; (d) 2.5 mol % $MgO-Al_2O_3$; (e) 30 mol % $MgO-Al_2O_3$; (f) 50 mol % $MgO-Al_2O_3$.

(26) Li, B.; Williams, G.; Rand, S. C.; Hinklin, T.; Laine, R. M. *Opt. Lett.* **2002**, *27*, 394.

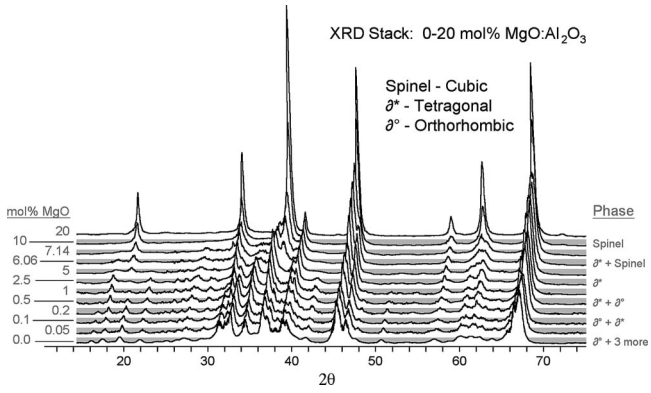

Figure 2. XRD powder patterns for $(MgO)_x(Al_2O_3)_{1-x}$ for $x = 0$–20 mol %.

FSP conditions as the high-viscosity alumatrane is replaced by the subliming $Mg(acac)_2$. In addition, even after filtering, there is a quantity of undissolved solids in the $Mg(acac)_2$ precursor, which may act as nucleation sites in the combustion stream. The exact impact on combustion parameters and conditions is unknown. This is still consistent with XRD and SSA results because both analysis methods are insensitive to the presence of a small portion of larger particles.

The particle morphologies observed in Figure 1 suggest the possibility of core–shell particle formation, but preliminary TEM analysis did not reveal any indication of a core–shell structure. Furthermore, the following sections discussing the XRD and DRIFT results will demonstrate that the as-produced alumina−magnesium aluminate spinel system is, in fact, a metastable solid solution with structural rearrangements as the site occupancy changes.

Powder XRD Patterns

XRDs of selected compositions in the $MgAl_2O_4-Al_2O_3$ phase field are given in Figure 2. The relevant ICDD cards are as follows: $MgAl_2O_4$, 73-1959; $MgAl_{26}O_{40}$, 20-0660; ∂^t-Al_2O_3, 16-394; $\partial°$-Al_2O_3, 46-1131; $\partial*$-Al_2O_3, 46-1215; θ-Al_2O_3, 23-1009. A gradual change in the XRD patterns is observed from pure alumina (Al_2O_3) through the stoichiometric magnesium spinel ($MgAl_2O_4$). Figure 3 graphs the percent of each phase present in the as-produced LF-FSP powders. Figure 4 uses cell refinement calculations (see the Experimental Section) based on the peak positions of the six strongest lines of the dominant phase to plot the lattice parameters of the *dominant* phase versus the composition.

The pure Al_2O_3 samples made by LF-FSP are a mixture of four transitional alumina phases: ∂^t, $\partial°$, $\partial*$, and θ. A more detailed analysis of these phases can be found elsewhere.[15] The amount of the nontetragonal transitional phases decreases with an increase in the MgO content. The addition of MgO stabilizes the ∂^t-Al_2O_3 phase because the Mg ions preferentially substitute for tetrahedrally coordinated Al^{3+} in the $\partial°$-Al_2O_3 lattice. The ∂^t-Al_2O_3 phase is isostructural with the $MgAl_{26}O_{40}$ phase previously identified by Lejus[27] as having a slightly larger unit cell because of the incorporation of the relatively large MgO tetrahedral and octahedral species.

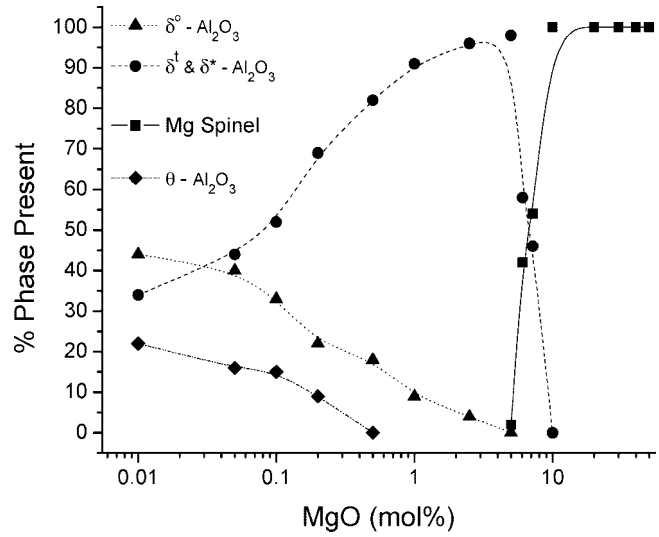

Figure 3. Dominant phase vs mol % MgO from calculations using Figure 2 data.

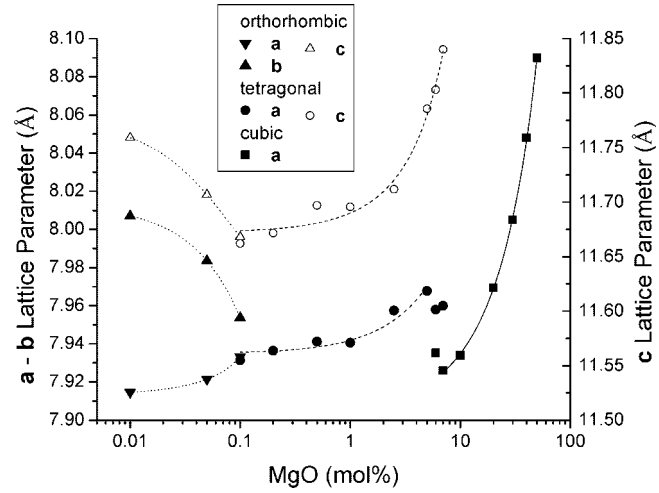

Figure 4. Lattice parameters of the dominant phase with an increase in the MgO concentration from calculations using Figure 2 data. Lines are linear fits to the data.

The stoichiometric magnesium aluminate ($MgAl_2O_4$) shows the expected phase pure spinel pattern, and the cubic spinel phase is preserved down to 10 mol % MgO. Samples with 7.17, 6.06, and 5 mol % MgO content begin to show peaks corresponding to the $MgAl_{26}O_{40}$ (∂^t) phase with a decrease in the $MgAl_2O_4$ phrase content with a decrease in the MgO content, until only the tetragonal phase is observed below 5 mol %. The thermodynamic phase diagram[28] depicts a wide spinel solid solution to arise at high temperatures (1400–2000 °C), extending down to ≈10 mol % MgO at the eutectic, while at standard temperature and pressure, the spinel solid solution is limited to 48–50 mol % MgO.

To our knowledge, there are no reports in the literature suggesting that the spinel structure along the $MgAl_2O_4-Al_2O_3$ tie-line remains stable to such low MgO contents. However, a thermodynamic revision of the $MgO-Al_2O_3$ diagram conducted by Hallstedt[28] suggests that the Al_2O_3 solvus extends to 11.4 mol % MgO at 2267 K. According

(27) Lejus, A. M. *Rev. Hautes Temp. Refract.* **1964**, *I*, 53, in French.

(28) Hallstedt, B. *J. Am. Ceram. Soc.* **1992**, *75*, 1497.

Table 2. Unit Cell Dimensions for Selected Transition Aluminas and the Relevant ICDD Cards ($MgAl_2O_4$, 73-1959; $MgAl_{26}O_{40}$, 20-0660; ∂^t-Al_2O_3, 16-394; $\partial°$-Al_2O_3, 46-1131; $\partial*$-Al_2O_3, 46-1215; θ-Al_2O_3, 23-1009)

	$\partial°$-Al_2O_3: 46-1215	$\partial*$-Al_2O_3: 46-1131	∂^t-Al_2O_3: 16-394	θ-Al_2O_3: 23-1009	$MgAl_{26}O_{40}$: 20-0660	$MgAl_2O_4$: 73-1959
	orthorhombic, *P*222 (No. 16)	tetragonal *P*4*m*2 (No. 115)	tetragonal, *I*	monoclinic, *C*2/*m*	tetragonal, *I*	cubic, *Fd*3*m* (No. 227)
a	7.934	5.599	7.934	5.625	7.956	8.05
b	7.956			2.906		
β				104.1		
c	11.711	23.657	23.657	11.813	11.745	

to Hallstedt's calculation, the solvus extends to a peritectic, where the minimum liquidus is at 16.4 mol % MgO at 2264 K. These calculations were based on a significant number of assumptions based on conflicting and sparse experimental data; therefore, the values should be seen as guides and not hard numbers. The development of a metastable phase at the eutectic composition is not unexpected.[29,30] The development of kinetic metastable phases follows the same phase rules as that of thermodynamically stable phases.

To best illustrate the phase development in the $MgAl_2O_4$−Al_2O_3 system, the structures will be explained as deviations from the stoichiometric $MgAl_2O_4$ spinel structure. In the ideal spinel structure, the oxygen atoms form a face-centered-cubic lattice where Al^{3+} occupies half of the octahedral sites and Mg^{2+} occupies one-eighth of the tetrahedral sites. It has been well documented that Mg^{2+} can also occupy the octahedral sites. The amount of octahedral occupancy is quantified as the degree of inversion. The degree of inversion found in natural and synthetic stoichiometric spinels can range from 0 to 40% based on the model by O'Neill and Navrotsky,[31] and typical degrees of inversion are from 15 to 30%.[32] Assuming an ideal structure, as the MgO content is reduced from the stoichiometric spinel, the Al^{3+} ions occupy an increasing number of tetrahedral positions. The Al^{3+} ions are accommodated in the tetrahedral positions, and the spinel structure is maintained to 10 mol % MgO.

Below 10 mol % MgO, a new metastable phase develops. This structure is a tetragonal distortion of the cubic spinel where the *c* axis is expanded by 50%. In the literature,[27] this phase is considered to be $MgAl_{20}O_{40}$ or 7.17 mol %, but the associated ICDD XRD crystal pattern is based on a unit cell with 48 oxygen atoms, which, assuming one Mg atom in the crystal structure, corresponds to $MgAl_{31}O_{47.5}[]_{0.5}$ or 6.06 mol %. This tetragonal structure is dominant until the MgO content decreases below 1 mol %, where an orthorhombic distortion of the tetragonal cell begins to develop and becomes dominant below 0.1 mol % MgO. The orthorhombic distortion is an expansion of one *a* axis and a contraction of the other (Figure 4). This distortion becomes larger as the MgO content decreases. These lattice calculations are based on a minimization of the sum of the squares calculations of a rather complex mixture of phases and do not correspond exactly with the published ICDD lattice parameters, but the graphed data fit Vegard's law well and true structures of transition aluminas are the subject of much speculation in the literature.[33–35]

Transition aluminas have often been referred to as consisting of distorted triple spinel unit cells.[36] The reported unit cell dimensions of selected transition aluminas are listed in Table 2. The powders used to determine the structures all have different methods of production and thermal histories. The complex nature of atomic diffusion and structural reordering in transition aluminas precludes any bulk sample from being homogeneous or representative. This topic was thoroughly reviewed by Levin and Brandon.[34] However, the family of phases or crystalline reflections, which exist between the well-defined γ- and α-aluminas, can be viewed as diffusion-limited structural relaxations dependent on surface energies, impurities, and thermal history.

DRIFT Spectra

DRIFT spectra of all samples are presented in Figure 5. Two main regions are of interest, 1100–400 and 4000−1500 cm^{-1}. The lower wavenumber region corresponds to typical ν(M−O) bands and the higher region to absorbed surface species. Absorbed surface water is present on the as-prepared samples in the 3600–3000 cm^{-1} spectral region as a series of overlapping ν(O−H) bands arising from both physisorbed and chemisorbed water. These as-prepared nanopowders have no significant organic species at the surface, as the absence of 2900–1700 cm^{-1} vibrations suggests.

Complementary to the following phase changes by XRD, it is possible to associate changes in the IR peak positions of the metal–oxygen stretches with the phases that form as the MgO content increases, as illustrated in Figure 6. The IR absorbances in the 760–840 cm^{-1} spectral region are associated with tetrahedral Al−O [ν(Al−O_t)]. The conversion from a predominantly orthorhombic to tetragonal structure above 0.1 mol % MgO (XRD in Figures 3 and 4) also results in a convergence of the 780 and 825 cm^{-1} peaks to a single peak, centered at 800 cm^{-1}. The ν(Al−O_t) bands are dominant from 0.1 to 6 mol % MgO, where the spinel structure begins to form. Between 6 and 10 mol % MgO, the ν(Al−O_t) band shifts back to 830 cm^{-1} and rapidly diminishes in intensity as the composition approaches the stoichiometric spinel.

The band centered at 725 cm^{-1}, which appears ≥5 mol %, is associated with tetrahedral Mg−O [ν(Mg−O_t)] in the spinel structure. The ν(Mg−O_t) intensity is inversely related to the intensity of the 830 cm^{-1} ν(Al−O_t) as the stoichiometric spinel is approached.

The 625 and 585 cm^{-1} spectral bands are associated with octahedral Al−O [ν(Al−O_o)]. In the pure alumina

(29) Levi, C. G. *Acta Mater.* **1998**, *46*, 787.
(30) Polli, A. D.; Lange, F. F.; Levi, C. G. *J. Am. Ceram. Soc.* **1996**, *79*, 1745.
(31) O'Neill, H.; Navrotsky, A. *Am. Mineral.* **1983**, *68*, 181.
(32) Andreozzi, G. B.; Princivalle, F.; Skogby, H.; Giusta, A. D. *Am. Mineral.* **2000**, *85*, 1164.
(33) Jayaram, V.; Levi, C. G. *Acta Metall.* **1989**, *37*, 569.
(34) Levin, I.; Brandon, D. *J. Am. Ceram. Soc.* **1998**, *81*, 1995.
(35) Cai, S. H.; Rashkeev, S. N.; Pantelides, S. T.; Sohlberg, K. *Phys. Rev. B* **2003**, *67*, 224104.
(36) Lippens, B. C.; de Boer, J. H. *Acta Crystallogr.* **1964**, *17*, 1312.

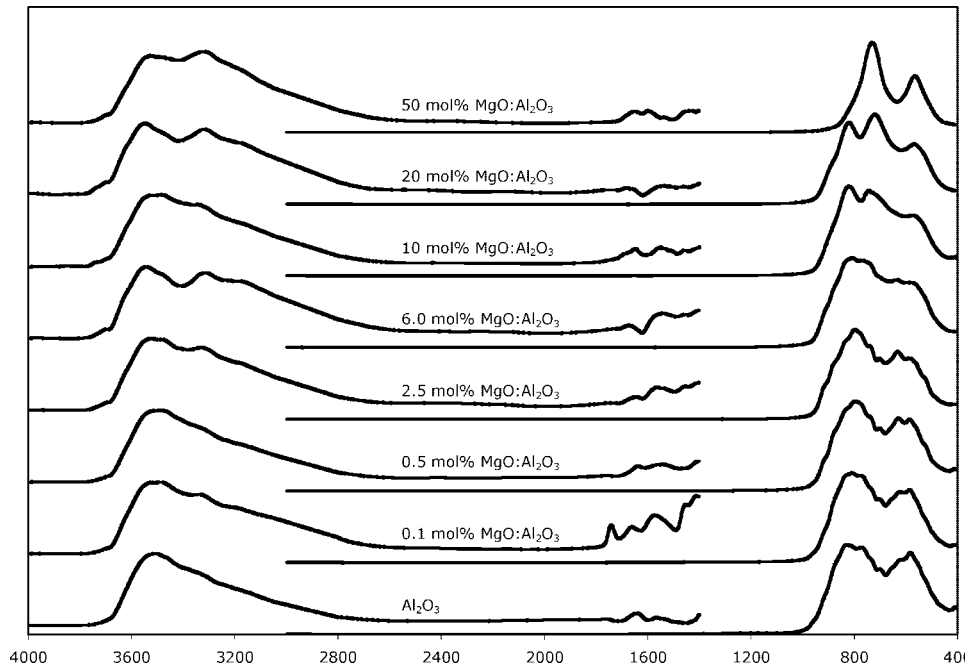

Figure 5. DRIFT spectra of selected samples along the $MgO-Al_2O_3$ tie-line.

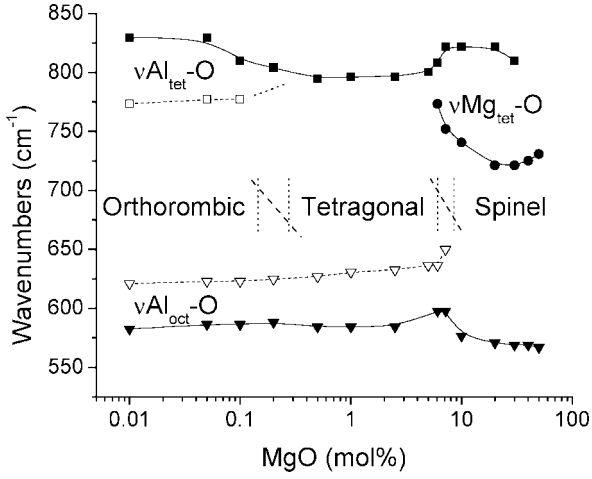

Figure 6. Changes in the dominant phase and ν(M−O) with the MgO content.

sample, the 625 cm^{-1} $\nu(Al-O_o)$ is of greater relative intensity than the 585 cm^{-1} band, but as the MgO content increases and the dominant structure changes from orthorhombic to tetragonal, the 585 cm^{-1} $\nu(Al-O_o)$ increases in relative intensity. The 625 cm^{-1} $\nu(Al-O_o)$ gradually changes in frequency from 620 to 630 cm^{-1} with an increase in the MgO content until the formation of the spinel phase, when the 625 cm^{-1} $\nu(Al-O_o)$ disappears. This suggests that there are two distinct octahedral positions in the orthorhombic and tetragonal structures and only a single position in the cubic spinel. The remaining $\nu(Al-O_o)$ rapidly decreases in frequency from 595 to 565 cm^{-1} as the composition approaches the stoichiometric spinel.

In the pure Al_2O_3 sample, water is present primarily as chemisorbed water, as evidenced by the comparatively narrow peak centered at 3500 cm^{-1}. As the MgO content increases, the absorption due to water broadens to include a second resolved peak centered at 3325 cm^{-1} and an unresolved peak near 3175 cm^{-1}. The relative intensities of the resolved peaks at 3500 and 3325 cm^{-1} do not change with composition. The change in the surface ν(O−H) bands offers the possibility of novel catalytic properties due to the associated change in Lewis site properties.[37]

Conclusions

We explored, systematically, the $Al_2O_3-MgAl_2O_4$ phase field to investigate metastable phase formation and optimize the resultant UV emission behavior (results not shown). The entire phase field was produced using two mutually soluble precursors: alumatrane and magnesium acetylacetonate. We were able to extend the magnesium spinel phase field to below 10 mol % MgO in Al_2O_3. As the content of MgO decreased below the eutectic (6–7 mol % MgO), the tetragonal δ-alumina was found to be the dominant phase. With MgO contents below 1 mol %, the orthorhombic δ-alumina phase formed. These transitions were corroborated by XRD and FTIR. This metastable extension of the spinel structure across the entire $Al_2O_3-MgAl_2O_4$ phase field at the nanoscale level creates the opportunity for new properties to be found in this well-studied system.

When viewed in terms of decreasing MgO content, the structural changes from the cubic spinel to tetragonal δ-alumina to orthorhombic δ-alumina are simple reorganizations of the spinel crystal structure. The continuous replacement of Al^{3+} in the tetrahedral (ideally Mg^{2+}) positions of the spinel structure results in shrinkage of the unit cell and loss of symmetry.

Supporting Information Available: Phase diagram, DTA peak positions and the corresponding Arrhenius plot activation energy, and powder XRD patterns. This material is available free of charge via the Internet at http://pubs.acs.org.

CM702388G

(37) Morterra, C.; Magnacca, G. *Catal. Today* **1996**, *27* (3–4), 497.